Radiometric Cross-Calibration of the ZY1-02D Hyperspectral Imager Using the GF-5 AHSI Imager

Chao Niu, Kun Tan, *Senior Member, IEEE*, Xue Wang, Bo Han, Shule Ge, Peijun Du, *Senior Member, IEEE*, and Feng Wang, *Member, IEEE*

***Abstract*— The ZY1-02D satellite, which was launched in 2019, is China's first civil hyperspectral satellite. However, the laboratory calibration and vicarious calibration methods could not provide accurate radiometric calibration coefficients after the satellite had been launched. In this article, we describe how a cross-calibration method was utilized to calibrate the ZY1-02D hyperspectral imager using the well-calibrated Gaofen-5 Advanced Hyperspectral Imager (GF-5 AHSI). The 6S radiative transfer model was selected to simulate the apparent reflectance of the two hyperspectral sensors under corresponding imaging conditions, and the calibration coefficients were calculated by spectral channel matching. The reflectance-based vicarious calibration was carried out for comparison. Through the validation experiments, it is shown that the reflectance data obtained by cross-calibration and vicarious calibration are basically consistent, showing a stable radiation performance. At the Dunhuang calibration site, the ratio of measured surface reflectance to the cross-calibrated image reflectance is between 0.9 and 1.1, the R^2 values are more than 0.96, and the spectral angles are less than 3°. The validation results for different ground features also show the applicability of the corrected coefficients. When compared with different sensors, the maximum difference between the ZY1-02D reflectance results after cross-calibration and Landsat-8/Sentinel-2 is less than 0.04 and the mean difference is less than 0.02, which further proves that the ZY1-02D hyperspectral imager has a high radiation accuracy after cross-calibration. The proposed cross-calibration method could be used as an effective supplement to the on-orbit calibration method and could also be extended to other satellite hyperspectral imagers.**

***Index Terms*— Cross-calibration, Gaofen-5 AHSI, radiometric calibration, vicarious calibration, ZY1-02D.**

Manuscript received August 23, 2021; revised October 27, 2021; accepted November 24, 2021. Date of publication November 30, 2021; date of current version February 25, 2022. This work was supported in part by the Natural Science Foundation of China under Grant 41871337 and Grant 42171335. *(Corresponding author: Kun Tan.)*

Chao Niu, Kun Tan, and Xue Wang are with the Key Laboratory of Geographic Information Science (Ministry of Education), the Key Laboratory of Spatial-Temporal Big Data Analysis and Application of Natural Resources in Megacities, Ministry of Natural Resources, and the School of Geographic Sciences, East China Normal University, Shanghai 200241, China (e-mail: tankuncu@gmail.com).

Bo Han is with the Institute of Remote Sensing Satellite, China Academy of Space Technology, Beijing 100094, China.

Shule Ge is with China Center for Resources Satellite Data and Application, Beijing 100094, China.

Peijun Du is with the Key Laboratory for Satellite Mapping Technology and Applications of NASG, Nanjing University, Nanjing 210023, China.

Feng Wang is with the Key Laboratory for Information Science of Electro-Magnetic Waves (MoE), Fudan University, Shanghai 200433, China.

Digital Object Identifier 10.1109/TGRS.2021.3131485

I. Introduction

With the development of high-resolution satellite technology, China has launched a series of remote sensing satellites carrying hyperspectral imagers. On May 9, 2018, China launched the Gaofen-5 (GF-5) satellite with the Advanced Hyperspectral Imager (AHSI) carried onboard. The AHSI imager features 330 spectral channels covering a solar reflective range of 400–2500 nm, with a spatial resolution of 30 m [1], and has been applied in the estimation of water quality parameters [2], leaf area index estimation [3], and the mapping of mangrove species [4]. On September 12, 2019, China launched the first civil hyperspectral satellite—ZY1-02D satellite. The ZY1-02D hyperspectral imager features 166 spectral channels and has a 60-km swath width. It has the same spectral range and spatial resolution as the AHSI imager. The ZY1-02D satellite was designed for the quantitative extraction and recognition of ground features in the process of geological and mineral exploration and land supervision, and can meet the requirements of large-scale and precise monitoring of multiple ecological elements.

The high spectral resolution of such imagers makes it possible to carry out a qualitative and quantitative environmental analysis, and accurate radiometric calibration can link the digital number (DN) to the radiance values, and these physical units are the basis of environmental parameter measurement [5]. Radiometric calibration is usually divided into prelaunch calibration and on-orbit calibration, which is carried out throughout the life cycle of the satellite [6]. Due to sensor normalizing to conditions in space and aging of the instrument, the radiometric coefficients obtained prelaunch are not applicable in the complex space environment, so on-orbit calibration needs to be carried out. On-orbit calibration methods include onboard calibration, vicarious calibration, and cross-calibration methods [7]. According to the different sources of radiation calibration, onboard calibration usually involves two methods: internal lamp calibration and sun calibration. The Landsat-5 Thematic Mapper (TM) and Landsat-7 Enhanced Thematic Mapper Plus (ETM+) sensors are equipped with an internal lamp calibrator, but the performance and stability of spaceborne lamps is limited, which has a great impact on the calibration accuracy [8], [9]. Moreover, the spectrum and intensity of the standard lamps are very much different from

1558-0644 © 2021 IEEE. Personal use is permitted, but republication/redistribution requires IEEE permission.
See https://www.ieee.org/publications/rights/index.html for more information.

Authorized licensed use limited to: East China Normal University. Downloaded on January 23,2024 at 02:06:19 UTC from IEEE Xplore. Restrictions apply.

the solar spectrum, which also increases the uncertainty of the calibration. However, the solar spectrum is relatively stable, and the solar irradiance spectrum has been determined, so an onboard calibration method based on a solar diffuser has been developed [10]. However, the solar diffuser attenuates in the space environment, resulting in the decline of the bidirectional reflectance distribution function (BRDF) accuracy. As a result, it is very difficult to monitor and correct the attenuation of diffuse reflectors. In addition, most sensors no longer include internal calibration, and we must use the vicarious calibration as a result. Vicarious calibration is the on-orbit calibration method to monitor the radiation performance and calibrate the deviation of calibration coefficients [11]. The reflectance-based vicarious calibration method is simple and effective, and it has commonly been utilized for the radiometric calibration of multispectral sensors such as SPOT-4 Vegetation (VGT) and Landsat-7 ETM+, and hyperspectral sensors such as the Advanced Land Imager (ALI) onboard the Earth Observing 1 (EO-1) satellite and the GF-5 AHSI [12]–[15]. However, vicarious calibration requires the selection of a suitable calibration area for *in situ* measurement and is limited by the field conditions and the high cost. After the launch of the ZY1-02D satellite, the weather and atmospheric conditions at the calibration site could not meet the requirements, and vicarious calibration could not be completed, which has affected the accuracy of the radiometric calibration and quantitative applications.

In order to solve these difficulties, cross-calibration methods have been proposed to replace *in situ* measurement by using concurrently collected images from a well-calibrated sensor. Cross-calibration has been successfully used for the Landsat-5 TM sensor, the Landsat-7 ETM+ sensor, the Gaofen-1 (GF-1) wide-field-view (WFV) sensor, and the Sentinel-2 Multispectral Instrument (MSI) [16]–[19].

There are three main categories of the cross-calibration methods: 1) ray-matching methods; 2) high spectral convolution methods; and 3) radiative transfer modeling methods [20]. The ray-matching methods use the coincident, co-angled, and co-located measurements, and compare and analyze the similar bands to obtain the relative gain coefficients. For example, Teillet *et al.* [16] proposed a radiometric cross-calibration method for the Landsat-5 TM sensor using the well-calibrated Landsat-7 ETM+ sensor as reference, and updated the calibration coefficient of Landsat-5 TM while incorporating adjustments for the spectral band differences. Li *et al.* [19] collected Sentinel-2 MSI and Landsat-8 Operational Land Imager (OLI) images during two simultaneous nadir overpasses in the Saharan desert, and calibrated the eight corresponding spectral bands. The calibration results showed that the radiometric difference of the seven corresponding bands was consistent to Landsat-8 OLI within 1%.

The high spectral convolution methods need the same observation conditions. Differing from the ray-matching methods, the high spectral convolution methods consider the radiation influence of the spectral response function and use the high spectral resolution data to improve the calibration accuracy [21]. The spectral band adjustment factor (SBAF), which takes into account the spectral profile of the target and the relative spectral responses, was proposed to compensate the intrinsic offsets in the radiometric cross-calibration of the Landsat-7 ETM+ sensor and the Moderate Resolution Imaging Spectroradiometer (MODIS) [22]. Gunshor *et al.* [23] calibrated the Geostationary Operational Environmental Satellite (GOES), Meteosat, MTSAT-IR, and Feng Yun (FY)-2C geostationary imagers using the high spectral resolution atmospheric infrared sounder (AIRS) as reference, in which spectral convolution between the different sensors and spectral gap filling for AIRS were considered.

The radiative transfer modeling methods establish the transformation relationship between the different sensors by using a radiation transmission model or field experiment, which can overcome the limitation of the observation conditions. For example, Green *et al.* [24] utilized the MODerate resolution atmospheric TRANsmission (MODTRAN) model to assess the on-orbit radiometric calibration of the EO-1 Hyperion instrument with Airborne Visible-Infrared Imaging Spectrometer (AVIRIS) measurements. In addition, the EO-1 Hyperion spectral calibration was assessed with a spectral fitting algorithm using the MODTRAN-modeled radiance spectra. Feng *et al.* [18] proposed a radiative transfer-based radiometric cross-calibration method for the GF-1 WFV instrument. The MODIS aerosol products and BRDF products have also been utilized to simulate the top of atmosphere (TOA) reflectance and correct the bidirectional effects, and the results have proved their accuracy in radiative transfer simulation.

For hyperspectral imagers, the spectral resolution is much higher than for multispectral imagers. In order to ensure the accuracy of cross-radiometric calibration, there is a higher requirement for the spectral resolution of the reference imagers. The spatial resolution and swath width of GF-5 AHSI imager we mentioned earlier are consistent with those of the ZY1-02D hyperspectral imager. In addition, GF-5 AHSI imager also has a higher spectral resolution. Accurate calibration coefficients for the GF-5 AHSI imager have been obtained using the vicarious calibration method, and the radiation error has been proven to be less than 5% by cross-validation [15]. The GF-5 AHSI imager can, therefore, be used as the reference sensor for the cross-calibration of the ZY1-02D hyperspectral imager. However, the difference of the image acquisition times between the two sensors is about one hour, and the imaging angle of the satellites also affects the TOA radiance, which in turn affects the accuracy of the radiometric cross-calibration.

In this article, we focus on providing timely and accurate radiometric calibration coefficient after satellite launch, so as to achieve normal qualitative and quantitative applications. Based on this, a radiative transfer modeling method was utilized to calibrate the ZY1-02D hyperspectral imager. In order to verify the radiometric accuracy of the cross-calibration, reflectance-based vicarious calibration was carried out at the Dunhuang calibration site of China. We also selected a uniform paddy field and bare soil area in Xuzhou, China, to verify the calibration results for different types of ground objects. In addition, multispectral images acquired by Landsat-8 and Sentinel-2 were also used for the multiple cross-validation.

Authorized licensed use limited to: East China Normal University. Downloaded on January 23,2024 at 02:06:19 UTC from IEEE Xplore. Restrictions apply.

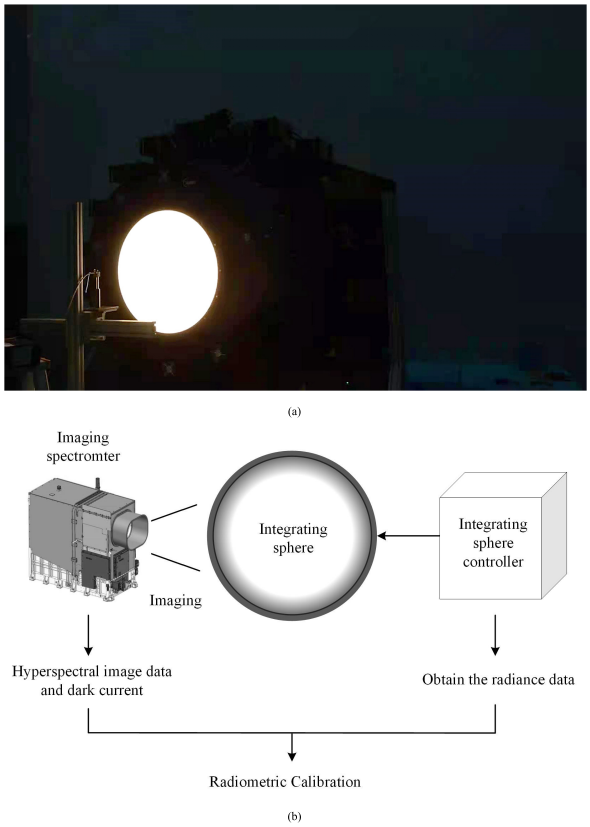

Fig. 1. Integrating sphere system. (a) Photography of laboratory calibration. (b) Schematic of integrating sphere system.

II. Data and Measurements

A. Sensor Laboratory Calibration

Sensor laboratory calibration is the basis of radiometric calibration. In this study, the integrating sphere system shown in Fig. 1 was used in the laboratory to determine the functional relationship between the DN output data and the radiance value. The radiometric calibration coefficients were obtained through the laboratory calibration of the sensor and were used to judge and evaluate the sensor radiation attenuation in orbit.

B. Calibration Sites

Cross-calibration requires different sensors to be imaging simultaneously in the same area, so that the selection of the calibration area directly affects the accuracy and effectiveness of the calibration results. Due to the recent launch times of the ZY1-02D and GF-5 satellites, the amount of data that can meet the cross-calibration conditions is very small. After data screening, we obtained a set of cross-calibration datasets for the Baotou calibration field. The Baotou calibration site was established to evaluate the radiation and spectral performance of airborne and satellite sensors. It is located at 40.88°N and 109.53°E in the Urad Qianqi area of Inner Mongolia in north China. The average altitude around the calibration site is about 1270 m, and the selected cross-calibration target shown in Fig. 2(a) is a semi-desert area with a typically clear sky and a uniform surface, and is thus less affected by the BRDF effect, making it an ideal calibration area [25].

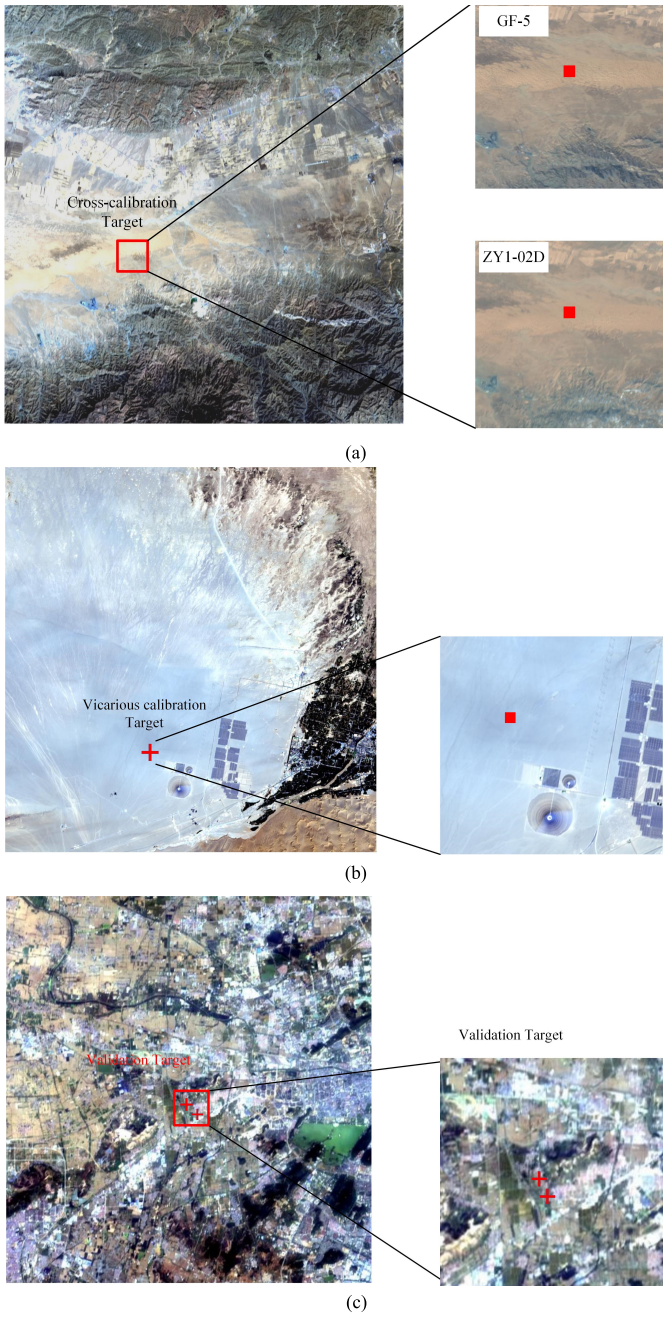

Fig. 2. Geographical locations of the calibration target and validation target. (a) Baotou cross-calibration site. (b) Dunhuang vicarious calibration site. (c) Xuzhou validation site.

In this study, we also chose the Dunhuang calibration site for the vicarious calibration to compare the results of the cross-calibration. The Dunhuang calibration site has been selected as a China Radiation Calibration Site (CRCS) since 1996. It is located at 40.18°N and 94.27°E in the Dunhuang, Gansu, China, and the elevation is approximately 1140 m. The calibration site is composed of flat gravel, fine sand, and a small amount of clay. The calibration target is shown in Fig. 2(b). The site has stable spectral characteristics due to its unique geographical and climatic conditions and plays an irreplaceable role in the field of in-orbit radiometric calibration and quantitative application [26].

Authorized licensed use limited to: East China Normal University. Downloaded on January 23,2024 at 02:06:19 UTC from IEEE Xplore. Restrictions apply.

TABLE I
COMPARISON OF THE PARAMETERS OF THE ZY1-02D HYPERSPECTRAL IMAGER AND THE GF-5 AHSI IMAGER

PARAMETER	ZY1-02D	GF-5
Orbit altitude (km)	778	705
Revisit period (days)	55	51
Ground sample distance (m)	30	30
Swath width (km)	60	60
Spectral range (μm)	0.4–2.5	0.4–2.5
Spectral resolution (nm)	VNIR: 10 SWIR: 20	VNIR: 5 SWIR: 10
Spectral bands	166	330
Accuracy of the absolute radiometric calibration	<7%	<5%
Accuracy of the relative radiometric calibration	<3%	<3%
SNR	⩾240 (0.4–0.9μm) ⩾180 (0.9–1.75μm) ⩾120 (1.75–2.50μm)	⩾200 (0.4–0.9μm) ⩾150 (0.9–1.75μm) ⩾100 (1.75–2.50μm)

C. Image Acquisition

The ZY1-02D and GF-5 satellites are both on sun-synchronous orbits, at orbit altitudes of 778 and 705 km, respectively, and their revisit period is 55 and 51 days, respectively. The fine spectrograms of the ZY1-02D hyperspectral imager are obtained at an interval of 10 nm for the visible and near-infrared (VNIR) region and 20 nm for the short-wave infrared (SWIR) region. The fine spectrograms of the GF-5 AHSI imager are obtained at an interval of 5 nm for VNIR and 10 nm for SWIR. In terms of the imaging quality, the ZY1-02D hyperspectral imager has a higher signal-to-noise ratio (SNR) than the GF-5 AHSI imager [27]. The imager parameters are listed in Table I.

A single hyperspectral image acquired by GF-5 and five hyperspectral images acquired by ZY1-02D were utilized for calibration and validation. Cross-calibration datasets were obtained at Baotou on March 26, 2020, by both GF-5 and ZY1-02D. Three datasets were obtained at Dunhuang on May 30, 2020, August 16, 2020, and August 19, 2020. One was used for the vicarious calibration and the other two for the validation. Another dataset to explore the calibration performance was obtained at Xuzhou on October 19, 2020. Furthermore, details of the hyperspectral images are provided in Table II.

In order to further prove the reliability of the calibration methods, a multiple cross-validation experiment using multispectral sensors was also carried out. The details of the images are shown in Table III.

D. In Situ Data Acquisition

The vicarious calibration method was utilized in the comparison, and synchronous meteorological parameters and ground reflectance data for the satellite imaging time were also acquired at the Dunhuang site. We utilized a Cimel CE318 sunphotometer to measure the aerosol optical depth (AOD) and water vapor.

At the Xuzhou validation site, we selected two large areas of pure ground objects, i.e., paddy field and bare soil, in the imaging center, and simultaneously obtained the ground spectra of these two kinds of ground objects. The atmosphere parameters in Xuzhou site were obtained by the observation data from the meteorological stations in Xuzhou, including water vapor, visibility, air temperature, humidity, and so on. The validation target is shown in Fig. 2(c).

III. METHOD

A. Cross-Calibration

According to the principle of radiation transmission, the relationship between the TOA reflectance and the TOA radiance can be expressed as follows [28]:

$$\rho_{\mathrm{TOA}}(\lambda) = \frac{\pi \cdot L(\lambda) \cdot d^2}{E_s(\lambda) \cdot \cos\theta_s} \tag{1}$$

where L is the TOA radiance, d is the earth–sun distance, θ_s is the solar zenith angle, and E_s is the solar radiation at the TOA.

For hyperspectral imagers, the values obtained in each channel are related to the spectral response function, so the solar radiation at the TOA in channel i can be calculated as follows:

$$E_{s,i} = \frac{\int S_i(\lambda) \cdot f(\lambda) d\lambda}{\int S_i(\lambda) d\lambda} \tag{2}$$

where S_i is the spectral response function of band i, and $f(\lambda)$ is the extra-atmospheric solar irradiance.

The differences in the observation geometry, time, meteorological conditions, and spectral response can affect the apparent radiance obtained. In this study, we considered the radiative transfer method for the cross-calibration and selected the 6S radiative transfer model to simulate the apparent reflectance of the two hyperspectral sensors under corresponding imaging conditions. In addition, as the viewing angles of the two sensors are small and can be regarded as vertical observation, and the calibration site has Lambertian reflection characteristics, the influence of the BRDF effect was not considered. The relationship between the reference sensor and the sensor to be calibrated can be obtained as follows:

$$\frac{L_C}{L_R} = \frac{\int_C S(\lambda) f_C(\lambda) d\lambda \cdot \int_R S(\lambda) d\lambda \cdot \rho_{\mathrm{TOA\_C}} \cdot \cos\theta_{S\_C}}{\int_R S(\lambda) f_R(\lambda) d\lambda \cdot \int_C S(\lambda) d\lambda \cdot \rho_{\mathrm{TOA\_R}} \cdot \cos\theta_{S\_R}}. \tag{3}$$

Due to the inconsistency of the channels and spectral response functions of the two sensors, spectral channel matching was required. Differing from multispectral sensors, hyperspectral sensors have hundreds of spectral channels, and the bandwidth of each channel is very narrow. The spectral response function of a hyperspectral sensor is generally obtained by function simulation according to the central wavelength and full width half maximum (FWHM). The commonly used spectral response functions are the impulse response function and the Gaussian response function, which

Authorized licensed use limited to: East China Normal University. Downloaded on January 23,2024 at 02:06:19 UTC from IEEE Xplore. Restrictions apply.

TABLE II
COMPARISON OF THE PARAMETERS OF THE ZY1-02D HYPERSPECTRAL IMAGER AND THE GF-5 AHSI IMAGER

	Cross-calibration		Vicarious calibration	Validation data		
Sensor	ZY1-02D	GF-5	ZY1-02D	ZY1-02D	ZY1-02D	ZY1-02D
Location	Baotou	Baotou	Dunhuang	Dunhuang	Dunhuang	Xuzhou
Acquisition time (UTC+8)	2020-03-26 11:48:20	2020-03-26 13:35:30	2020-08-16 12:58:38	2020-05-30 12:47:56	2020-08-19 12:55:14	2020-10-19 11:13:15
Center coordinates	40.6097°N, 109.4888°E	40.6761°N, 109.5183°E	40.2387°N, 94.3978°E	40.1524°N, 94.4158°E	40.2043°N, 94.4236°E	34.3761°N, 116.9996°E
Solar zenith	40.5074°	39.7827°	28.6389°	21.3693°	29.7333°	45.6578°
Solar azimuth	156.8624°	198.9681°	155.1019°	145.1236°	154.4966°	164.9247°
Satellite zenith	0.9223°	0.0783°	13.9535°	3.6660°	8.4601°	4.0920°
Satellite azimuth	122.2906°	158.7035°	281.3698°	106.4609°	280.4054°	103.1672°

TABLE III
DETAILS OF THE SELECTED LANDSAT 8 AND SENTINEL-2 IMAGES

Sensor	Location	Acquisition time (UTC+8)	Center coordinates	Solar zenith	Solar azimuth
Landsat-8	Dunhuang	2020-06-02,12:19:33	40.2958°N,95.0648°E	65.503°	131.756°
		2020-08-21,12:20:06	40.2931°N,95.0644°E	56.307°	141.547°
	Xuzhou	2020-10-24,10:43:05	34.5566°N,118.0283°E	40.737°	157.570°
Sentinel-2	Dunhuang	2020-05-29,12:37:11	40.1375°N, 94.8194°E	21.372°	145.955°
		2020-08-19,12:37:26	40.1375°N, 94.8194°E	31.203°	147.196°
	Xuzhou	2020-06-25,11:08:28	33.8875°N, 117.5623°E	45.978°	164.297°

are expressed as follows:

$$S_{\text{impulse}}(\lambda) = \begin{cases} 1, & \lambda = \lambda_i \\ 0, & \lambda \neq \lambda_i \end{cases} \tag{4}$$

$$S_{\text{gaussian}}(\lambda) = \frac{1}{\sqrt{2\pi}\sigma} e^{\frac{-(\lambda-\lambda_i)^2}{2\sigma^2}} \tag{5}$$

$$\sigma = \frac{\text{FWHM}}{2\sqrt{2\ln 2}} \tag{6}$$

where λ_i is the central wavelength, and σ can be calculated by the FWHM. Because of the high spectral resolution of the two hyperspectral imagers, we selected the impulse response function for the spectral channel matching. The input TOA radiance and TOA reflectance of the reference sensor can be interpolated by a cubic spline function to have the same channel and spectral response as the sensor to be calibrated. According to (3), the TOA radiance of the sensor to be calibrated can be expressed as follows:

$$L_{i,C} = L_{i,R} \frac{\rho_{i,\text{TOA\_}C} \cdot \cos\theta_{S\_C}}{\rho_{i,\text{TOA\_}R} \cdot \cos\theta_{S\_R}} \tag{7}$$

where $L_{i,c}$ and $\rho_{i,\text{TOA\_}C}$ are, respectively, the TOA radiance and TOA reflectance of the sensor to be calibrated in channel i. $L_{i,R}$ and $\rho_{i,\text{TOA\_}R}$ are, respectively, the TOA radiance and TOA reflectance of the reference sensor after interpolation in channel i.

The relationship between the DN value and the TOA radiance can be expressed as follows:

$$L_i = a_i DN_i + b_i \tag{8}$$

where a_i is the gain coefficient in band I and b_i is the offset value in band i. In this study, the hyperspectral images we obtained had been preprocessed by dark current subtraction, and the offset value of each band was 0. The gain value of each band of the ZY1-02D hyperspectral imager can be expressed as follows:

$$a_{i,C} = \frac{L_{i,C}}{DN_{i,C}}. \tag{9}$$

B. Vicarious Calibration

Reflectance-based vicarious calibration was used to compare and verify the accuracy of the cross-calibration method. Among the reflectance-based calibration methods, we selected the MODTRAN model to simulate the TOA radiance by inputting the surface reflectance, atmospheric parameters, and observation parameters. After field investigation, a uniform part in the Dunhuang calibration site was selected for experiments. The surface reflectance was measured by using a Spectra Vista Corporation (SVC) spectroradiometer, and the direct solar irradiance and sky diffuse radiance using a Cimel CE318 sunphotometer within half an hour before and after the overpass ZY1-02D satellite.

The vicarious calibration method we used was proposed by Tan *et al.* [15], which was successfully applied to GF-5 AHSI imagers. If we assume that the surface cover is uniform Lambertian, the TOA radiance can be expressed as follows:

$$L = L_p + \frac{\rho_s}{1 - S\rho_s} F_d T(\theta_v) \tag{10}$$

Authorized licensed use limited to: East China Normal University. Downloaded on January 23,2024 at 02:06:19 UTC from IEEE Xplore. Restrictions apply.

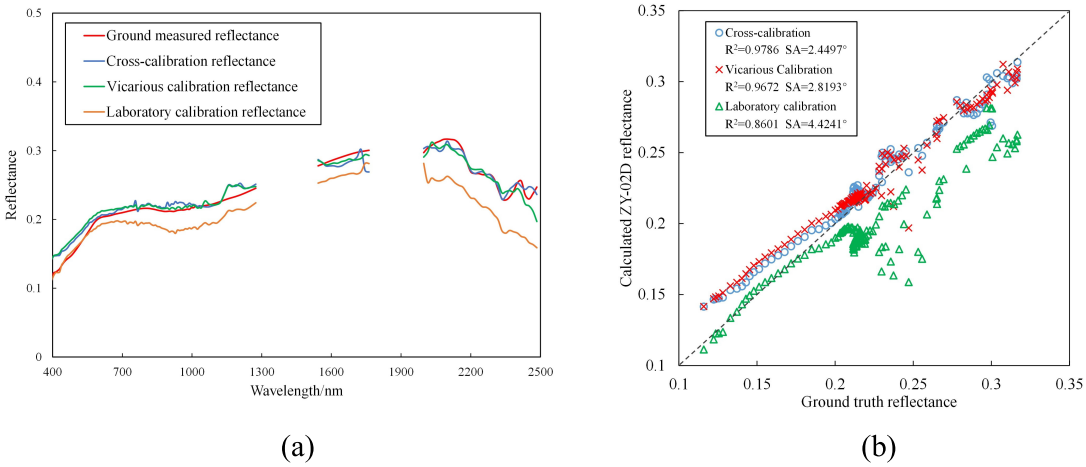

Fig. 3. Calibration results and the ground-measured reflectance at the Dunhuang site on May 30, 2020. (a) Spectral curves of the surface reflectance result from 400 to 2500 nm. (b) Scatter plots and accuracies of the three calibration results.

where L_p is the path radiance, ρ_s is the surface reflectance, S is the spherical albedo of the atmosphere, F_d is the total downward solar radiation, $T(\theta_v)$ is the atmospheric transmittance, and θ_v is the cosine of the view zenith angle. Then, ρ_s can be expressed as follows:

$$\rho_s = \frac{L - L_p}{F_d T(\theta_v) + (L - L_p)S}. \tag{11}$$

When the observation conditions are known, the MODTRAN model outputs the corresponding TOA radiance values by inputting the constant surface reflectance. Here, we define $F = F_d T(\theta_v)$. There are three unknown parameters in (10): F, L_p, and S, and these parameters can be calculated by inputting three different ρ_s values in MODTRAN model. Finally, the TOA radiance L can be calculated using the measured surface reflectance value in Dunhuang calibration site.

After extracting and calculating the average DN value, the vicarious calibration gain value of each band of the ZY1-02D hyperspectral imager can be expressed as follows:

$$\text{Gains}_i = \frac{L_i}{DN_i}. \tag{12}$$

C. Validation Analysis

The accuracy of the calibration results can be validated by comparing the atmospherically corrected hyperspectral image reflectance with the measured surface reflectance. The calibration result can be evaluated by the determination coefficient R^2. The spectral angle can be used to evaluate the similarity between the corrected spectrum and the ground object spectrum

$$\cos\alpha = \frac{\vec{\mathbf{t}} \cdot \vec{\mathbf{r}}}{\|\vec{\mathbf{t}}\| \times \|\vec{\mathbf{r}}\|} = \frac{\sum_{i=1}^{n} t_i r_i}{\sqrt{\sum_{i=1}^{n} t_i^2} \times \sqrt{\sum_{i=1}^{n} r_i^2}} \tag{13}$$

where n is the number of bands, $\vec{\mathbf{t}} = (t_1, t_2, \ldots, t_n)$ is the calibrated image reflectance, and $\vec{\mathbf{r}} = (r_1, r_2, \ldots, r_n)$ is the ground-measured reflectance. a is the spectral angle in the range of 0°–90°. The lower spectral angle means higher spectral similarity. In general, spectral angles less than 0.3 radians (17.2°) can be considered highly similar.

In addition, the ratio of the measured surface reflectance to the calibrated image reflectance can be calculated to indicate the consistency and fluctuation at different spectral channels. The ratio is calculated as follows:

$$\text{Ratio} = \frac{\text{Ground measured Ref}}{\text{Calibrated image Ref}}. \tag{14}$$

IV. Results

A. Dunhuang Validation Results

After radiometric calibration using the cross-calibration coefficients and vicarious calibration coefficients, the surface reflectance was obtained through atmospheric correction. In addition, the surface reflectance result obtained using the laboratory radiometric calibration coefficients was also used for judging and evaluating the sensor radiation attenuation. Fig. 3 shows the comparison results obtained at the Dunhuang site on May 30, 2020, by the three different calibration methods and the ground-measured reflectance after removing the water vapor bands. It can be seen that the calibration reflectance spectra for the ZY1-02D imager show a high degree of consistency at the Dunhuang site. Mathematically, a higher R^2 means that the calibration result agrees well with the measured reflectance. On the contrary, a lower spectral angle means a higher similarity between spectra, which means the model has a better performance. The accuracy of the laboratory calibration result is the lowest, with the R^2 value being 0.8601 and the spectral angle being 4.4241° between the measured reflectance and the results. For the cross-calibration result, the R^2 value is 0.9786 and the spectral angle is 2.4497° between the measured reflectance and the cross-calibration results, which represents a better performance than the vicarious calibration. Fig. 4 shows the comparison results obtained at the Dunhuang site on August 19, 2020. The cross-calibration reflectance spectra are also highly consistent with the ground-measured reflectance. The R^2 value is 0.9681 and the spectral

Authorized licensed use limited to: East China Normal University. Downloaded on January 23,2024 at 02:06:19 UTC from IEEE Xplore. Restrictions apply.

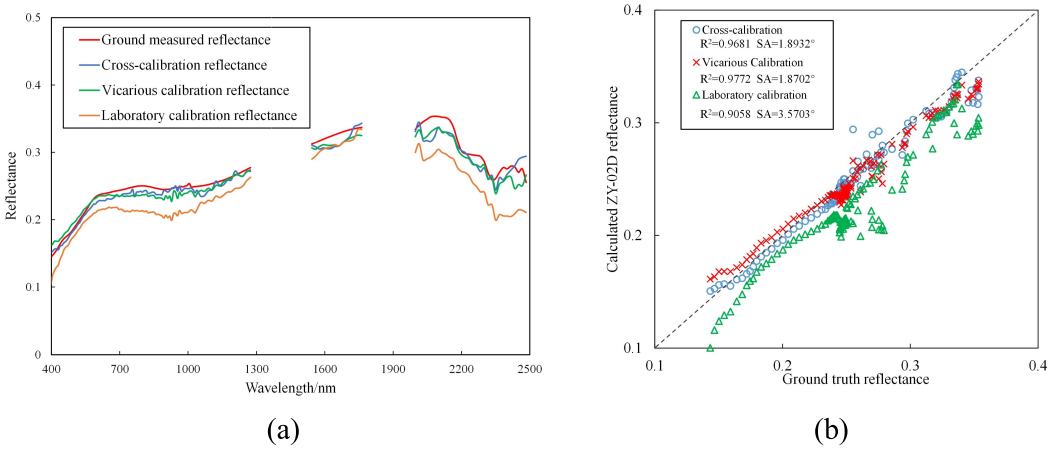

Fig. 4. Calibration results and the ground-measured reflectance at the Dunhuang site on August 19, 2020. (a) Spectral curves of the surface reflectance result from 400 to 2500 nm. (b) Scatter plots and accuracies of the three calibration results.

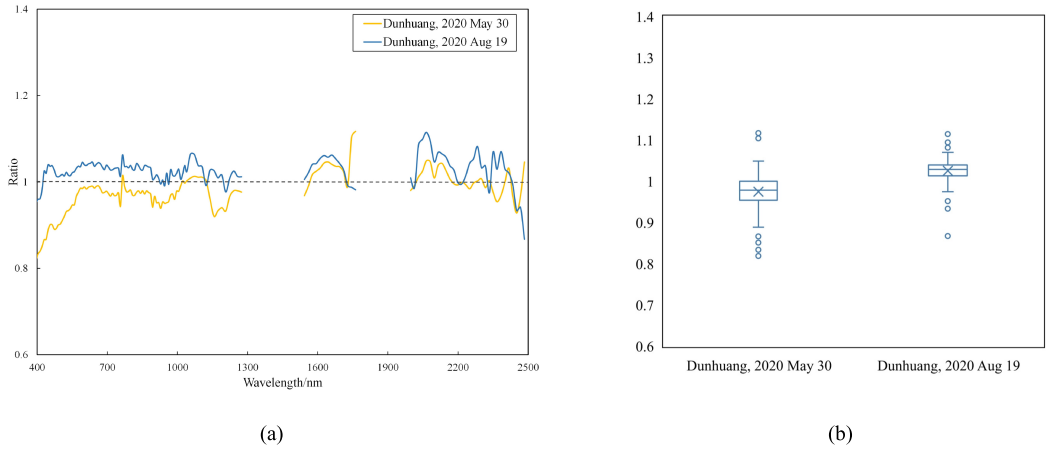

Fig. 5. Ratio of the ground-measured reflectance to the calibrated ZY1-02D surface reflectance at the Dunhuang site. (a) Ratio curves of the two Dunhuang site datasets. (b) Box plots with distribution.

angle is 1.8932° between the measured reflectance and the cross-calibration results, so the accuracy is similar to that of the vicarious calibration results.

Fig. 5(a) shows the ratio of the ground-measured reflectance to the ZY1-02D cross-calibration surface reflectance at the Dunhuang site. Fig. 5(b) shows a box plot showing the distribution of the ratio. This shows that all the spectral channels are between 0.9 and 1.1, except for a few outliers, and most are between 0.95 and 1.05, which is consistent with the measurements and proves the validity of the calibration.

B. Xuzhou Validation Results

To verify the performance of the calibration coefficients for different types of ground features, we carried out the verification of the results in two different land-cover types: paddy field and bare soil. Figs. 6 and 7 show the results of the three different calibration methods for the ground-measured paddy field and bare soil reflectance after removing the water vapor bands at the Xuzhou site on October 19, 2020. From the trend of the spectral curve and the extreme value of reflectance, the reflectance results of ZY1-02D are basically consistent with the measured reflectance. However, due to the limitation of the spatial resolution, the selected objects are affected by mixed pixels and the heterogeneous ground objects, resulting in deviation of the reflectance in some channels. For the cross-calibration result for the paddy field, the R^2 value is 0.9648 and the spectral angle is 6.1898°. The R^2 value of the cross-calibration result for bare soil is 0.9183 and the spectral angle is 4.2983°. The deviation between the laboratory calibration reflectance and the measured reflectance is again the largest. The results of the cross-validation for these two ground features are slightly better than those of the vicarious calibration, which shows the reliability of the proposed cross-calibration method.

Fig. 8 shows the ratio curves and box plots for the two ground features. The ratio for the bare soil is relatively stable, and the ratio values are around 1.0. The ratio for the paddy field fluctuates at 400–500 nm and 2000–2200 nm, but more than half is still between 0.9 and 1.1, which means that the calibrated reflectance is highly consistent with the ground-measured reflectance.

Authorized licensed use limited to: East China Normal University. Downloaded on January 23,2024 at 02:06:19 UTC from IEEE Xplore. Restrictions apply.

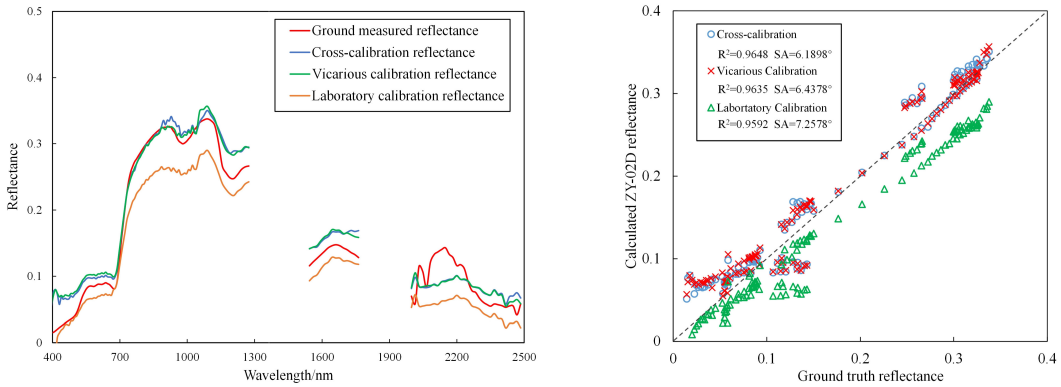

(a) (b)

Fig. 6. Calibration results for the paddy field category and the ground-measured reflectance at the Xuzhou site on October 19, 2020. (a) Spectral curves of the surface reflectance result from 400 to 2500 nm. (b) Scatter plots and accuracies of the three calibration results.

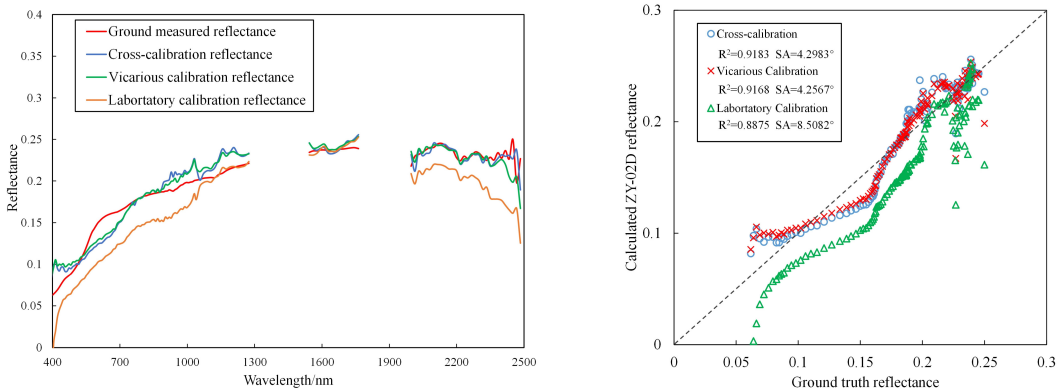

(a) (b)

Fig. 7. Calibration results for the bare soil category and the ground-measured reflectance at the Xuzhou site on October 19, 2020. (a) Spectral curves of the surface reflectance results from 400 to 2500 nm. (b) Scatter plots and accuracies of the three calibration results.

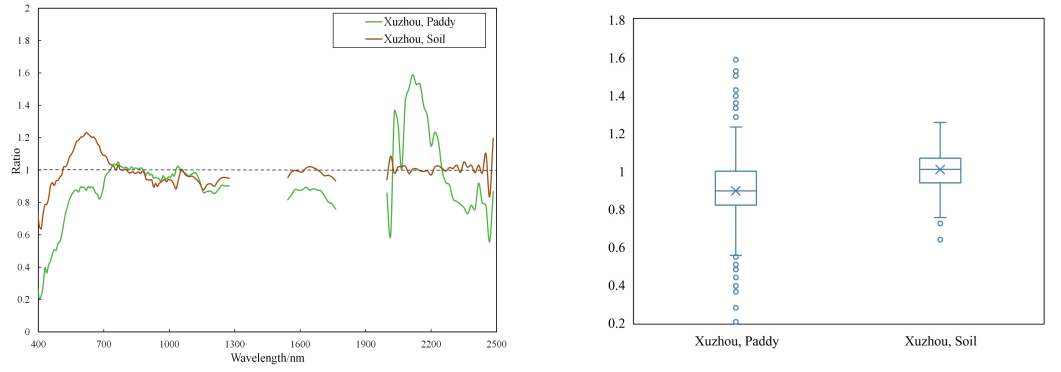

(a) (b)

Fig. 8. Ratio of the ground-measured reflectance to the calibrated ZY1-02D surface reflectance at the Xuzhou site. (a) Ratio curves for the two different features. (b) Box plots with distribution.

C. Comparison With Different Sensors

In addition to comparing the cross-calibration results with the real surface reflectance, multispectral sensors were used for cross-validation and further performance assessment. The reflectance results of the cross-calibration and the Landsat-8 and Sentinel-2 sensors are shown in Fig. 9. The cross-calibration reflectance of the ZY1-02D imager is highly consistent with the Landsat reflectance and Sentinel reflectance. We compared the central wavelengths corresponding to each band of Landsat-8 and Sentinel-2 with the reflectance values of the ZY1-02D imager after interpolation, and calculated the difference values, as shown in Table V.

Authorized licensed use limited to: East China Normal University. Downloaded on January 23,2024 at 02:06:19 UTC from IEEE Xplore. Restrictions apply.

TABLE IV
COMPARISON OF THE RESULTS OF THE DIFFERENT CALIBRATION METHODS

Validation site	Ground feature	Calibration method	R^2	Spectral angle°
Dunhuang 30 May 2020	Calibration site	Cross-calibration	0.9786	2.4497
		Vicarious calibration	0.9672	2.8193
		Laboratory calibration	0.8601	4.4241
Dunhuang 19 August 2020	Calibration site	Cross-calibration	0.9681	1.8932
		Vicarious calibration	0.9772	1.8702
		Laboratory calibration	0.9058	3.5703
Xuzhou 19 October 2020	Paddy field	Vicarious calibration	0.9648	6.1898
		Laboratory calibration	0.9635	6.4378
		Laboratory calibration	0.9592	7.2578
Xuzhou 19 October 2020	Bare soil	Vicarious calibration	0.9183	4.2983
		Laboratory calibration	0.9168	4.2567
		Laboratory calibration	0.8875	8.5082

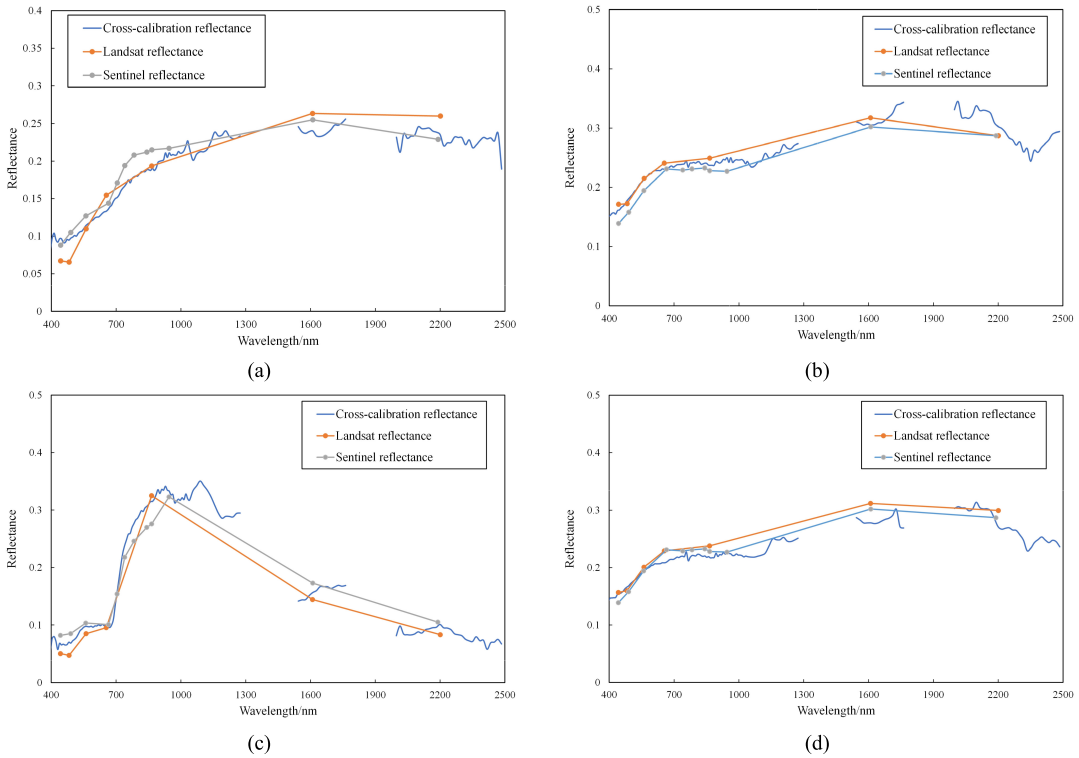

Fig. 9. Reflectance results of the cross-calibration and the multispectral sensors at the different sites. (a) Dunhuang site on May 30, 2020. (b) Dunhuang site on August 19, 2020. (c) Paddy field at the Xuzhou site. (d) Bare soil at the Xuzhou site.

The mean difference is under 0.02, and the maximum difference is under 0.04. The comparison results show that the ZY1-02D hyperspectral imager is highly consistent with the Landsat-8 and Sentinel-2 sensors, which further show that the ZY1-02D hyperspectral imager has a high radiation accuracy after cross-calibration.

V. DISCUSSION

Due to the influence of weather factors at the calibration site, vicarious calibration could not be completed in time after the launch of the ZY1-02D satellite. In addition, the radiometric coefficients obtained in a laboratory environment are not applicable in a complex space environment. Under the premise of ensuring the radiation accuracy of the reference sensor, the cross-calibration method can effectively make up for the limitations of the laboratory calibration and vicarious calibration methods, and can be used to obtain accurate calibration coefficients for the sensor.

The proposed radiative transfer modeling cross-calibration method considered the radiation difference caused by different imaging time and imaging angle between the reference sensor and the sensor to be calibrated. Compared with the vicarious calibration method, the accuracy difference is less than 2%. With the increase of the number of hyperspectral satellites and the improvement of the sensors' performance, this cross-calibration method could also be extended to other satellite hyperspectral imagers.

In this study, there is a small difference between the corrected reflectance and the ground-measured reflectance. Here, we mainly discuss two possible errors. First, the inaccurate atmospheric state will lead to atmospheric model inaccuracy, for example, water vapor residuals at 1140 nm, path radiance,

Authorized licensed use limited to: East China Normal University. Downloaded on January 23,2024 at 02:06:19 UTC from IEEE Xplore. Restrictions apply.

TABLE V
DIFFERENCE BETWEEN THE ZY1-02D IMAGER AND LANDSAT-8/SENTINEL-2

Sensor	Location and image acquisition time	Maximum difference	Minimum difference	Mean difference
Landsat-8	Dunhuang (30 May 2020)	0.0340	0.0026	0.0168
	Dunhuang (19 August 2020)	0.0153	0.0015	0.0094
	Xuzhou-paddy (19 October 2020)	0.0229	0.0030	0.0137
	Xuzhou-soil (19 October 2020)	0.0302	0.0041	0.0197
Sentinel-2	Dunhuang (30 May 2020)	0.0241	0.0013	0.0113
	Dunhuang (19 August 2020)	0.0231	0.0033	0.0133
	Xuzhou-paddy (19 October 2020)	0.0388	0.0033	0.0169
	Xuzhou-soil (19 October 2020)	0.0289	0.0075	0.0160

and scattering from the surround in the blue region of the spectrum [29]. In addition, the different absorption paths measured by the sunphotometer versus the satellite spectrometer may cause discrepancies, resulting in deviation of atmospheric correction results. Second, the adjacency effects result from the scattering of radiation reflected from surrounding pixels into the sensor field of view and further introduce uncertainty into the atmospheric correction [30]. For example, the calibration results for the bare soil at the Xuzhou site in Fig. 7 shows a "red edge" at 720 nm, which indicated that the vegetation around this pixel has an impact on the soil spectrum.

In addition, we have noticed that that the laboratory calibration results appear superior to the vicarious and cross-calibration results in the shortest wavelengths at Dunhuang site on 30, May 2020, shown in Fig. 3(a), and vegetation at Xuzhou site shown in Fig. 6(a). One possible reason is hypothesized: the atmospheric path radiation in the blue region of the spectrum and inaccurate atmospheric state has a certain impact on the radiative transfer model [31], resulting in the high calibration reflectance results in the range of 400–500 nm. Due to the low calibration coefficient in the laboratory, the reflectance increases after atmospheric correction, which just leads to the laboratory results being closer to the ground-measured reflectance than the corrected results.

Nevertheless, two major limitations should be discussed. First, cross-calibration site is a semi-desert area with a typically clear sky and a uniform surface, and the view zenith angles for the reference and calibrated sensors are relatively small; the BRDF effects are negligible. But for the wide-field-of-view sensors, the uncertainty caused by BRDF effects is about 5% [18]. Second, there is more than an hour time difference in overpass time. Some studies have counted the mean difference of multiple overpass to determine the uncertainty on Sentinel-2 TOA reflectance, and the error due to 30 min difference in overpass times is less than 0.2% in the worst Sentinel-2 bands [32]. Due to the stable meteorological conditions of the cross-calibration field, only the imaging conditions were taken into consideration in the radiative transfer model, and the change of meteorological conditions is not considered.

VI. CONCLUSION

In this study, the GF-5 AHSI imager with a high spectral resolution after precise radiometric calibration was utilized for the cross-calibration of the ZY1-02D hyperspectral imager, and the calibration results were compared with those of the laboratory calibration method and vicarious calibration method. The reliability of the cross-calibration method was verified using multiple measured surface reflectance datasets. It was found that the results of the laboratory calibration are no longer suitable for the space environment, and the calculated reflectance was found to be quite different from the measured surface reflectance. The ZY1-02D hyperspectral imager calibrated by both the cross-calibration method and the vicarious calibration method showed a stable radiometric performance. The ratio of the measured surface reflectance to the cross-calibrated image reflectance was between 0.9 and 1.1, except for a few outliers, at the Dunhuang site, the R^2 values are more than 0.96, and the spectral angles are less than 3°. The verification results for different types of ground features at Xuzhou showed that the R^2 values were 0.9648 and 0.9183 and the spectral angles were 6.1898° and 4.2983° for the paddy field and bare soil, respectively.

The results of the cross-calibration and vicarious calibration were similar. In the four groups of validation experiments, three groups of experiments reported a cross-calibration result that was better than the vicarious calibration result, which shows the reliability of the cross-calibration method. In addition, through a comparison with different sensors, the maximum difference between the ZY1-02D reflectance results after cross-calibration and Landsat-8/Sentinel-2 was found to be less than 0.04, and the mean difference was less than 0.02, which further proved that the ZY1-02D hyperspectral imager had a high radiation accuracy after the cross-calibration. In the future, we will consider predicting the overlapping imaging area in advance and will collect the meteorological data and the spectral data *in situ* for accurate calibration and verification.

ACKNOWLEDGMENT

The authors would like to thank the Institute of Remote Sensing Satellite, China Academy of Space Technology, for providing the data used in the experiments.

REFERENCES

[1] Y. N. Liu *et al.*, "The advanced hyperspectral imager aboard China's GaoFen-5 satellite," *IEEE Geosci. Remote Sens. Mag.*, vol. 7, no. 4, pp. 23–32, Dec. 2019.

Authorized licensed use limited to: East China Normal University. Downloaded on January 23,2024 at 02:06:19 UTC from IEEE Xplore. Restrictions apply.

[2] Y. Liu, C. Xiao, J. Li, F. Zhang, and S. Wang, "Secchi disk depth estimation from China's new generation of GF-5 hyperspectral observations using a semi-analytical scheme," *Remote Sens.*, vol. 12, no. 11, p. 1849, Jun. 2020.

[3] Z. Chen *et al.*, "Leaf area index estimation algorithm for GF-5 hyperspectral data based on different feature selection and machine learning methods," *Remote Sens.*, vol. 12, no. 13, p. 2110, Jul. 2020.

[4] L. Wan, Y. Lin, H. Zhang, F. Wang, M. Liu, and H. Lin, "GF-5 hyperspectral data for species mapping of mangrove in Mai Po, Hong Kong," *Remote Sens.*, vol. 12, no. 4, p. 656, Feb. 2020.

[5] S. Liang, *Quantitative Remote Sensing of Land Surfaces*. Hoboken, NJ, USA: Wiley, 2005.

[6] G. Chander, B. L. Markham, and J. A. Barsi, "Revised Landsat-5 thematic mapper radiometric calibration," *IEEE Geosci. Remote Sens. Lett.*, vol. 4, no. 3, pp. 490–494, Jul. 2007.

[7] M. Dinguirard and P. N. Slater, "Calibration of space-multispectral imaging sensors: A review," *Remote Sens. Environ.*, vol. 68, no. 3, pp. 194–205, 1999.

[8] G. Chander and B. Markham, "Revised Landsat-5 TM radiometric calibration procedures and postcalibration dynamic ranges," *IEEE Trans. Geosci. Remote Sens.*, vol. 41, no. 11, pp. 2674–2677, Nov. 2003.

[9] G. Chander, X. Xiong, T. Choi, and A. Angal, "Monitoring on-orbit calibration stability of the Terra MODIS and Landsat 7 ETM+ sensors using pseudo-invariant test sites," *Remote Sens. Environ.*, vol. 114, no. 4, pp. 925–939, Apr. 2010.

[10] E. Heck, K. M. de Beurs, B. C. Owsley, and G. M. Henebry, "Evaluation of the MODIS collections 5 and 6 for change analysis of vegetation and land surface temperature dynamics in north and South America," *ISPRS J. Photogramm. Remote Sens.*, vol. 156, pp. 121–134, Oct. 2019.

[11] X. Xiong, J. Sun, X. Xie, W. L. Barnes, and V. V. Salomonson, "On-orbit calibration and performance of aqua MODIS reflective solar bands," *IEEE Trans. Geosci. Remote Sens.*, vol. 48, no. 1, pp. 535–546, Jan. 2010.

[12] P. M. Teillet *et al.*, "A generalized approach to the vicarious calibration of multiple Earth observation sensors using hyperspectral data," *Remote Sens. Environ.*, vol. 77, no. 3, pp. 304–327, 2001.

[13] K. J. Thome, "Absolute radiometric calibration of Landsat 7 ETM+ using the reflectance-based method," *Remote Sens. Environ.*, vol. 78, nos. 1–2, pp. 27–38, Oct. 2001.

[14] S. F. Biggar, K. J. Thome, and W. Wisniewski, "Vicarious radiometric calibration of EO-1 sensors by reference to high-reflectance ground targets," *IEEE Trans. Geosci. Remote Sens.*, vol. 41, no. 6, pp. 1174–1179, Jun. 2003.

[15] K. Tan *et al.*, "Vicarious calibration for the AHSI instrument of Gaofen-5 with reference to the CRCS Dunhuang test site," *IEEE Trans. Geosci. Remote Sens.*, vol. 59, no. 4, pp. 3409–3419, Apr. 2021.

[16] P. M. Teillet, J. L. Barker, B. L. Markham, R. R. Irish, G. Fedosejevs, and J. C. Storey, "Radiometric cross-calibration of the Landsat-7 ETM+ and Landsat-5 TM sensors based on tandem data sets," *Remote Sens. Environ.*, vol. 78, nos. 1–2, pp. 39–54, 2001.

[17] N. Mishra, M. Haque, L. Leigh, D. Aaron, D. Helder, and B. Markham, "Radiometric cross calibration of Landsat 8 Operational Land Imager (OLI) and Landsat 7 Enhanced Thematic Mapper Plus (ETM+)," *Remote Sens.*, vol. 6, no. 12, pp. 12619–12638, Dec. 2014.

[18] L. Feng, J. Li, W. Gong, X. Zhao, X. Chen, and X. Pang, "Radiometric cross-calibration of Gaofen-1 WFV cameras using Landsat-8 OLI images: A solution for large view angle associated problems," *Remote Sens. Environ.*, vol. 174, no. 1, pp. 56–68, Mar. 2016.

[19] S. Li, S. Ganguly, J. L. Dungan, W. Wang, and R. R. Nemani, "Sentinel-2 MSI radiometric characterization and cross-calibration with Landsat-8 OLI," *Adv. Remote Sens.*, vol. 6, no. 2, p. 147, 2017.

[20] G. M. Jiang, H. Yan, and L. L. Ma, "Intercalibration of SVISSR/FY-2C infrared channels against MODIS/Terra and AIRS/Aqua channels," *IEEE Trans. Geosci. Remote Sens.*, vol. 47, no. 5, pp. 1548–1558, May 2009.

[21] M. M. Gunshor, T. J. Schmit, and W. P. Menzel, "Intercalibration of the infrared window and water vapor channels on operational geostationary environmental satellites using a single polar-orbiting satellite," *J. Atmos. Ocean. Technol.*, vol. 21, no. 1, pp. 61–68, 2004.

[22] G. Chander *et al.*, "Applications of spectral band adjustment factors (SBAF) for cross-calibration," *IEEE Trans. Geosci. Remote Sens.*, vol. 51, no. 3, pp. 1267–1281, Mar. 2013.

[23] M. M. Gunshor, T. J. Schmit, W. P. Menzel, and D. C. Tobin, "Intercalibration of broadband geostationary imagers using AIRS," *J. Atmos. Ocean. Technol.*, vol. 26, no. 4, pp. 746–758, Apr. 2009.

[24] R. O. Green, B. E. Pavri, and T. G. Chrien, "On-orbit radiometric and spectral calibration characteristics of EO-1 Hyperion derived with an underflight of AVIRIS and *in situ* measurements at Salar de Arizaro, Argentina," *IEEE Trans. Geosci. Remote Sens.*, vol. 41, no. 6, pp. 1194–1203, Jun. 2003.

[25] N. Wang *et al.*, "Ground-based automated radiometric calibration system in Baotou site, China," *Proc. SPIE*, vol. 10427, Oct. 2017, Art. no. 104271J.

[26] X. Hu *et al.*, "Characterization of CRCS Dunhuang test site and vicarious calibration utilization for Fengyun (FY) series sensors," *Can. J. Remote Sens.*, vol. 36, no. 5, pp. 566–582, Oct. 2010.

[27] H. Y. Zhang, B. Han, X. H. Wang, M. An, and Y. Lei, "Hyperspectral camera system index argument and system design of ZY-1-02D satellite," *Spacecraft Eng.*, vol. 29, no. 6, pp. 10–18, 2020.

[28] B.-C. Gao, K. B. Heidebrecht, and A. F. H. Goetz, "Derivation of scaled surface reflectances from AVIRIS data," *Remote Sens. Environ.*, vol. 44, nos. 2–3, pp. 165–178, 1993.

[29] L. C. Sanders, J. R. Schott, and R. Raqueño, "A VNIR/SWIR atmospheric correction algorithm for hyperspectral imagery with adjacency effect," *Remote Sens. Environ.*, vol. 78, no. 3, pp. 252–263, 2001.

[30] R. Houborg and M. F. McCabe, "Impacts of dust aerosol and adjacency effects on the accuracy of Landsat 8 and RapidEye surface reflectances," *Remote Sens. Environ.*, vol. 194, pp. 127–145, Jun. 2017.

[31] Y. J. Kaufman, "Aerosol optical thickness and atmospheric path radiance," *J. Geophys. Res., Atmos.*, vol. 98, no. D2, pp. 2677–2692, Feb. 1993.

[32] J. Gorroño, A. C. Banks, N. P. Fox, and C. Underwood, "Radiometric inter-sensor cross-calibration uncertainty using a traceable high accuracy reference hyperspectral imager," *ISPRS J. Photogramm. Remote Sens.*, vol. 130, pp. 393–417, Aug. 2017.

Chao Niu received the B.S. degree in geographic information science and the M.S. degree in photogrammetric and remote sensing from China University of Mining and Technology, Xuzhou, China, in 2017 and 2020, respectively. He is currently pursuing the Ph.D. degree in cartography and geographic information system with East China Normal University, Shanghai, China.

His research interests include the hyperspectral image processing and quantitative inversion of water quality parameters.

Kun Tan (Senior Member, IEEE) received the B.S. degree in information and computer science from Hunan Normal University, Hunan, China, in 2004, and the Ph.D. degree in photogrammetric and remote sensing from China University of Mining and Technology, Jiangsu, China, in 2010.

From September 2008 to September 2009, he was a Joint Ph.D. Student of remote sensing with Columbia University, New York, NY, USA. From 2010 to 2018, he was with the Department of Surveying, Mapping and Geoinformation, China University of Mining and Technology. He is currently a Professor with the Key Laboratory of Geographic Information Science (Ministry of Education), East China Normal University, Shanghai, China. His research interests include hyperspectral image classification and detection, spectral unmixing, quantitative inversion of land surface parameters, and urban remote sensing.

Xue Wang received the B.S. degree in geographic information system and the Ph.D. degree in photogrammetric and remote sensing from China University of Mining and Technology, Xuzhou, China, in 2014 and 2019, respectively.

He is currently a Post-Doctoral Researcher with the Key Laboratory of Geographic Information Science (Ministry of Education), East China Normal University, Shanghai, China. His research interests include hyperspectral imagery processing, deep learning, and ecological monitoring.

Authorized licensed use limited to: East China Normal University. Downloaded on January 23,2024 at 02:06:19 UTC from IEEE Xplore. Restrictions apply.

Bo Han received the B.S. degree in electronic measurement from Branch of Beihang University, Beijing, China, in 1985.

He has been a Vice-Chief Designer of ZY-1 series (CBERS) remote sensing satellite in China Academy of Space Technology since 2008. His research interest includes hyperspectral device application in space.

Shule Ge received the B.S. degree in electronic science and technology and Ph.D. degree in optical engineering from Beijing Institute of Technology, Beijing, China, in 2005 and 2010, respectively.

He is currently a Researcher with China Center for Resources Satellite Data and Application, Beijing. His research interests include processing and calibration of hyperspectral and multispectral remote sensing data, atmospheric lidar data processing, and hyperspectral image classification.

Peijun Du (Senior Member, IEEE) received the Ph.D. degree in geodesy and survey engineering from China University of Mining and Technology, Xuzhou, China, in 2001.

He is currently a Professor of remote sensing and geographical information science with Nanjing University, Nanjing, China. He has published more than 70 articles in international peer-reviewed journals and more than 100 papers in international conferences and Chinese journals. His research interests focus on remote sensing image processing and pattern recognition, hyperspectral remote sensing, and applications of geospatial information technologies.

Dr. Du was a member of Scientific Committee or Technical Committee of other international conferences, including WHISPERS (2010–2016), URBAN (2011, 2013, and 2015), MultiTemp (2011, 2013, and 2015), ISIDF 2011, and SPIE European Conference on Image and Signal Processing for Remote Sensing (2012–2016). He was an Associate Editor of IEEE GEOSCIENCE AND REMOTE SENSING LETTERS. He also served as the Co-Chair for the Technical Committee of URBAN2009, IAPR-PRRS 2012, EORSA2014, IEOAs 2015, and CCGC2015, and the Co-Chair for the Local Organizing Committee of JURSE 2009, WHISPERS 2012, and EORSA 2012.

Feng Wang (Member, IEEE) received the B.S. and M.S. degrees from Information Engineering University, Zhengzhou, China, in 2006 and 2010, respectively, and the Ph.D. degree from Fudan University, Shanghai, China, in 2017.

He was an Assistant Research Fellow with Shanghai Institute of Technical Physics, Chinese Academy of Sciences, Shanghai. He is an Assistant Professor with the Key Laboratory for Information Science of Electromagnetic Waves (MoE), Fudan University. His research interests include radar imaging, hyperspectral remote sensing, and target recognition.

Authorized licensed use limited to: East China Normal University. Downloaded on January 23,2024 at 02:06:19 UTC from IEEE Xplore. Restrictions apply.